Confinement of a β-barrel protein in nanoperforated free-standing nanomembranes for ion transport

Anna Puiggalí-Jou,[1,2] Maria M. Pérez-Madrigal,[1,2,*] Luis J. del Valle,[1,2] Elaine Armelin,[1,2] María T. Casas,[1] Catherine Michaux,[3] Eric A. Perpète,[3] Francesc Estrany,[2,4] and Carlos Alemán[1,2,*]

[1] *Departament d'Enginyeria Química, ETSEIB, Universitat Politècnica de Catalunya, Avda. Diagonal 647, Barcelona E-08028, Spain*

[2] *Center for Research in Nano-Engineering, Universitat Politècnica de Catalunya, Campus Sud, Edifici C', C/Pasqual i Vila s/n, Barcelona E-08028, Spain*

[3] *Laboratoire de Chimie Physique des Biomolécules, Unité de Chimie Physique Théorique et Structurale (UCPTS), University of Namur, Rue de Bruxelles, 61, 5000 Namur, BELGIUM.*

[4] *Departament d'Enginyeria Química, Escola Universitària d'Enginyeria Tècnica Industrial de Barcelona, Universitat Politècnica de Catalunya, Comte d'Urgell 187, 08036 Barcelona, Spain*

[*] m.mar.perez@upc.edu and carlos.aleman@upc.edu

ABSTRACT

Bioinspired free-standing nanomembranes (FSNMs) for selective ion transport have been tailored by immobilizing the Omp2a β-barrel membrane protein inside nanoperforations created in flexible poly(lactic acid) (PLA) nanomembranes. Perforated PLA FSNMs have been prepared by spin-coating a 99:1 PLA:poly(vinyl alcohol) mixture, and through a phase segregation process nanofeatures with dimensions similar to the entire nanomembrane thickness (~110 nm) were induced. These nanofeatures have subsequently been transformed into nanoperforations (diameter: ~51 nm) by selective solvent etching. The protein confined inside the nanopores of PLA FSNMs preserves the β-barrel structure and organizes in ovoid aggregates. The transport properties of Na^+, K^+, and Ca^{2+} across non-perforated PLA, nanoperforated PLA, and Omp2a-filled nanoperforated PLA have been monitored by measuring the nanomembrane resistance with electrochemical impedance spectroscopy (EIS). The incorporation of nanoperforations enhances the transport of ions across PLA nanomembranes, whereas the functionality of immobilized Omp2a is essential to exhibit effects similar to those observed in biological nanomembranes. Indeed, Omp2a-filled nanoperforated PLA nanomembranes exhibit stronger affinity towards Na^+ and Ca^{2+} ions than towards K^+. In summary, this work provides a novel bioinspired strategy to develop mechanically stable and flexible FSNMs with channels for ion transport precisely located inside artificial nanoperforations, thus holding great potential for applications in biofiltration and biosensing.

INTRODUCTION

Biological ion channels, which smartly control the movement of ions and small molecules into and out of the cell, have inspired scientists to build materials with applications in nanofluidics,[1,2] molecule and ion filters,[3,4] as well as biosensors.[5,6] Amongst the many approaches addressing selective ion transport, considerable efforts have recently been devoted to mimic the principles and functions of channels contained in biological nanomembranes (NMs).[7-11]

Biological membranes are made of lipid bilayers and embedded proteins sensing and subsequently controlling the exchange of substances between the cell and its environment. For instance, ion channels are self-assembled proteins that selectively transport ions through the cell membrane, while porin proteins are water-filled open channels allowing the passive penetration of hydrophilic molecules.[12] The latter are typically found as monomers or trimers in the outer membranes of Gram-negative bacteria, as well as in mitochondria[13] and chloroplast[14] of eukaryotic cells. Gram-negative bacteria surround themselves with a second outer membrane (OM) playing the role of an effective barrier. That is, this OM is even more hydrophobic than a typical phospholipid membrane due to the presence of lipopolysaccharides, whereas the translocation of hydrophilic species across OMs is mainly governed by the presence of porins.[15]

In this work, the attention is focused on the trimeric OM protein Omp2a from *Brucella melitensis*.[16] This β-barrel protein, which is formed by a sequence of 367 amino acids, allows the passive diffusion of small molecular weight hydrophilic materials (< 667 Da) across the OM (*e.g.* ions, nutrients, and drugs). Although neither the function of Omp2a nor the 3D structure of the channel is fully described, structural

studies suggested that Omp2a first refolds under a monomeric form (39 KDa) and then self-associates into a trimeric state (115 KDa).[17,18]

Supporting biological channels like porins, onto biological or synthetic polymeric bilayers presents limitations for practical applications due to their limited mechanical strength and stability.[19-22] Synthetic solid state membranes offer several advantages over bilayer-based approaches, such as mechanical stability, control over pore dimension and shape, and modifiable surfaces for desired functions.[8,23] Within this context, we recently examined ion diffusion through Omp2a immobilized in a supported poly(N-methylpyrrol) (PNMPy) membrane.[24] Electrical impedance spectroscopy (EIS) studies evidenced that Omp2a promotes the passive transport of K^+ and Na^+ in solutions with relatively high ionic concentrations, preferentially favouring the diffusion of hydrated Na^+ with respect to that of hydrated K^+.[24] Unfortunately, some drawbacks were also identified for such system. For instance, PNMPy membranes electrochemically synthesized were not self-standing, a stainless steel support being used to electropolymerize PNMPy. Furthermore, the porin immobilization and orientation were not well-controlled. In addition, the membrane thickness (219±71 nm) was much higher than both the height of the porin (~5 nm)[12] and the thickness of conventional biological lipid bilayers (2-5 nm).[25] Consequently, the passive ion transport was not only due to Omp2a, but assisted by PNMPy, which is known to be an electrochemically active polymer.[26,27]

A few studies have reported track-etched polymeric membranes with nanopores as solid support of ion channels, despite complex chemical processes were frequently involved in the fabrication of such systems.[8,28,29] For the selective biomolecular recognition through metal···protein specific interactions, Ali *et al.*[8] constructed a nanobiosensor based on the immobilization of metal terpyridine complexes inside

nanopores, which were fabricated in polyethylene terephthalate membranes using asymmetric chemical etching. Guo *et al.*[28] also presented a single-pore nanofluidic energy-harvesting system that efficiently converts Gibbs free energy in the form of a salinity gradient into electricity. Experiments were conducted on ion-track-etched single nanopores embedded in polyamide membranes of 12 μm in thickness, which were irradiated with a single swift heavy ion and subsequently submitted to chemical etching. Balme *et al.*[7] filled nanopores (diameter= 15 nm) of commercial track-etched polycarbonate films (thickness= 5 μm) with the ion channel gramicidin A (GA). Unfortunately, such membranes did not exhibit the expected properties in terms of ion permeability and selectivity, which was attributed to the fact nanopores were not fully filled with GA, and therefore ions diffused in the "free" electrolyte confined inside the nanopore instead of directly interacting with GA.

Here, we have prepared poly(lactic acid) (PLA) free-standing nanomembranes (FSNMs) with nanopores crossing the entire ultra-thin film thickness as solid support, then loading the Omp2a porin for selective ion transport. Nanoperforations have been obtained using spin-coating combined with phase segregation processes in immiscible PLA:poly(vinyl alcohol) (PVA) mixtures, and subsequently removing PVA domains via selective solvent etching.[29] The immobilization of Omp2a not only at the surface, but also inside the nanopores, which has been achieved by incubating nanoperforated PLA NMs in protein solutions, has led to important changes in the physical properties of nanoperforated PLA NMs, including their electrochemical impedance response towards different electrolytic media.

RESULTS

Protein characterization. The Omp2a protein was expressed, purified, and refolded using a previously reported procedure,[17,24] which is briefly described in the ESI. The isoelectric point of Omp2a, which contains 367 amino acids (Table S1), is 4.47. The monomeric and trimeric association of refolded Omp2a was investigated by sodium dodecyl sulfate polyacrylamide gel electrophoresis (SDS-PAGE). Primary and secondary bands were observed at ~39 and ~115 kDa (Figure S1), suggesting that the trimeric form was less populated than the monomeric species. The competition between monomer···monomer and monomer···SDS interactions provides a possible explanation for the low self-association of the monomers to form the trimeric units.

Dynamic light scattering (DLS) measurements reflected that in the buffer solution used to maintain Omp2a (see ESI), SDS molecules form small micelles with an effective diameter D_{eff}= 5.7±0.1 nm (Figure S2) that increases to D_{eff}= 6.4±0.4 nm upon the addition of the protein. This increment has been associated with the incorporation of the Omp2a monomer to the SDS micelles. In contrast, aggregates with D_{eff}= 228±38 nm are observed when the protein is diluted in phosphate buffered saline (PBS) solution. The formation of these aggregates has been attributed to the de-protection of the hydrophobic zones of the protein (trans-membrane), which induces the self-association process. According to these results, the SDS-containing buffer medium was not changed during protein deposition onto nanoperforated membranes.

Despite the complete transformation of protein population into trimers has not been achieved, the secondary structure of the protein was well-preserved. This is evidenced by Figure S3, which compares the circular dichroism (CD) spectra recorded for Omp2a in four different scenarios: (i) heated 5 min at 90 ºC, (ii) just after being defrosted (as-obtained), (iii) after four days of incubation, and (iv) after being deposited onto the NMs (see below). In all cases, with the exception of the heated protein, the spectra

featured a broad minimum about 217 nm that is typically associated with β-stranded proteins.[30] It is well-known that changes in temperature can produce modifications in its structure. As a negative control the solution temperature was increased to 90 ºC where the conformational lost was observed. The heated protein solution exhibits a significant decrease in the depth and width of the far-UV CD spectra.

TEM micrographs from Omp2a solutions stained with 2% uranyl acetate enabled us to identify not only trimeric units, but also higher hierarchical structures formed by around 6-8 trimeric units due to self-association processes (Figures 1 and S4). All these structures have been attributed to the hydrophobic interactions promoted by the side groups at the external side of the β-barrels, consistently with the effective diameter measured by TEM for the trimers (D_{eff}= 9.3±3.0 nm) and such bigger aggregates (D_{eff}= 25.9±4.8 nm), respectively.

Nanoperforated PLA nanomembrames. Nanoperforated PLA FSNMs were prepared using an already described two-step procedure:[29] (1) spin-coating a mixture of PLA and poly(vinyl alcohol) (PVA), which are immiscible polymers but both soluble in 1,1,1,3,3,3-hexafluoroisopropanol (HFIP), onto a PVA sacrificial layer to form the appropriated nanofeatures (*i.e.* phase separation domains with dimensions similar to the entire film thickness); and (2) selective solvent etching using milliQ water to dissolve both the PVA sacrificial layer and the PVA domains of PLA-PVA NMs, consequently transforming such nanofeatures into nanoperforations. Perforated FSNMs were initially obtained by considering 90:10 and 99:1 PLA:PVA v/v mixtures. Details about the whole preparation process are described in the ESI.

Figure 2a displays 3D AFM height images coloured with phase skin of NMs obtained using 99:1 PLA:PVA mixtures. Briefly, AFM phase imaging registers phase

signal shifts due to changes in the adhesion force between the tip and the surface, thus being sensitive to the surface mechanical and viscoelastic properties (*i.e.* stiffness/softness). Accordingly, AFM phase information allows for the chemical mapping of polymer composites. Hence, Figure 2a illustrates how the PVA nanophases, which are clearly identified in PLA-PVA NMs as yellow domains, disappear after selective water etching while PLA phase remains (dark purple domain). The elimination of PVA in NMs obtained from both 90:10 and 99:1 mixtures was also followed by FTIR spectroscopy (Figure S5). For perforated and non-perforated PLA NMs, Table 1 lists the average diameter of the nanopores (ϕ), the root-mean-square roughness (Rq) values of 5×5 μm^2 surface areas and film thickness (L), which also corresponds to the depth of the pores. It is evidenced that Rq increases rapidly with the content of PVA in the polymer mixture. Hence, the formation of nanopores provokes drastic topographic alterations with respect to the ultra-flat non-perforated PLA NMs. In contrast, L remains almost unchanged for perforated and non-perforated NMs, the influence of PVA-induced nanofeatures being negligible in this case.

SEM and AFM micrographs provided in Figure 2b display nanometric details of perforated PLA FsNMs derived from 99:1 PLA:PVA mixture, while micrographs of non-perforated PLA (used as a control) are displayed in Figure S6. The diameter of the nanopores as determined from SEM micrographs is 65±32 nm and 51±22 nm for NMs originating from 90:10 and 99:1 mixtures, respectively. As the effective diameter of Omp2a aggregates determined by TEM range from 9.3±3.0 nm to 25.9±4.8 nm, PLA NMs with the smallest pore diameter have been selected for immobilizing the OM protein. Moreover, AFM observations, which recorded simultaneously surface structure (height) and material composition (phase data) allow us to verify the presence of PLA region only (*i.e.* no phase contrast), thus indicating complete removal of PVA domains.

Finally, Figure 2c shows a digital camera image of a nanoperforated PLA FSNM floating in water. These self-standing ultra-thin films are very flexible and robust, and they can be easily folded into small shapes.

Omp2a-Filled nanoperforated PLA nanomembrames. Nanoperforated PLA NMs supported onto ITO and prepared using 99:1 PLA:PVA mixtures, were placed on a 24-well plate and incubated with 500 µL of 0.5, 0.25 or 0.125 mg/mL Omp2a solution for 48 h with slight agitation (80 rpm) at room temperature. Then, NMs samples were rinsed three times with milliQ water to remove residues.

The incorporation of Omp2a preserving its β-barrel structure as proved by CD (Figure S3), induces drastic changes in the physical properties of nanoperforated PLA NMs (Figure 3a). Indeed, the wettability significantly increases upon the incorporation of the protein. Although the contact angle (CA) of PLA and nanoperforated PLA (CA= 78º±6º and 72º±7º, respectively) is just below the threshold value that separates hydrophilic and hydrophophic surfaces (*i.e.* CA ≤ 90º and CA > 90º, respectively), the CA of Omp2a-filled NMs is only 24º±14º. Similarly, the Rq (5×5 μm^2 surface area) of nanoperforated PLA NMs increases from 21±3 nm to 27±5 nm after Omp2a deposition. In order to explain these physical changes, nanoperforated PLA NMs were investigated by SEM (Figure 3b) and AFM (Figure 3c). Low and high magnification SEM micrographs, as well as AFM images reveal the presence of aggregates at the surface of PLA NMs, which has been attributed to protein agglomeration. However, these aggregates are significantly bigger than the pure Omp2a assemblies observed by TEM from stained solutions (Figure 1), precluding an unambiguous identification. In opposition, height and phase AFM images (Figures 3c and S7) evidence the presence of aggregates both on the surface and inside the pores. Although phase contrast is not as

enhanced as in Figure 2a, topographical and texture differences reveal the existence of different phases (see below Figure 4a). Furthermore, the dimensions of these aggregates are very varied, ranging from some hundreds to a few tenths of nanometers. Cross sectional profiles of the interior of the pores indicate that their dimensions are suitable to host protein not only as aggregates of trimers (Figure 1), but also as individual trimers and monomers. Furthermore, both the roughened topography of the nanopore walls and the hydrophobic character of PLA favour the physical immobilization of Omp2a, no chemical treatment being required for such purpose. On the other hand, it is worth noting that β-barrel porins typically present a significant oval shape,[31] which is preserved in the aggregates observed by both SEM and AFM (Figure 3c).

Besides, comparison of the 3D AFM height images coloured with phase skin surfaces recorded before and after incubation with Omp2a allows confirming the presence of adsorbed oval protein aggregates around and inside the nanopores (Figure 4a). Specifically, phase information clearly distinguishes Omp2a domains (*i.e.* dark purple aggregates) from the PLA region they are adsorbed onto, which is coloured in green. The average diameter of such immobilized Omp2a aggregates is 27±5 nm (Figure 4b), which is in excellent agreement with the effective diameter measured by TEM for aggregates (26±5 nm in Figure 1). Furthermore, the average height of these aggregates is 6±2 nm (Figure 4c), which is fully consistent with the ~6 nm in height identified for the majority of β-barrel porins studied so far.[31]

The Omp2a retention efficiency (RE), expressed as the ratio (in %) between the mass of protein entrapped on the nanoperforated PLA substrate and the mass of Omp2a in the incubation solution, was evaluated using the Bradford assay. Figure 4d displays the amount of immobilized protein per unit of area and the RE for both perforated and non-perforated NMs. Results indicate higher the concentration of protein in the incubation

solution, the greater the amount of immobilized protein. On the contrary, the highest RE (5.8±1.0%:) was obtained for the incubation solution with the lowest concentration of protein (0.12 mg/mL), while RE values derived after using the 0.5 and 0.25 mg/mL protein solutions were practically identical (2.9±0.7% and 2.8±1.3%, respectively). This feature indicates that the protein saturation limit is reached at 0.25 mg/mL. Interestingly, the amount of immobilized protein and RE are very low (*i.e.* 0.4±0.3 μg/cm^2 and 0.3±0.2%, respectively) for the non-perforated PLA NMs. This feature clearly indicates that, although Bradford assays do not distinguish between proteins adsorbed onto the surface of the nanofilm or confined inside the pores, the amount of protein immobilized inside the latter is significantly higher. Thus, the adsorption of protein onto the surface is difficult because of the smoothness at non-perforated regions (*i.e.* Rq is 1.7±0.2 nm for non-perforated NMs), while the roughness inside the nanoperforations (Figure 3c) is large enough to facilitate the confinement of the protein. It is well known that physical immobilization of protein aggregates on ultra-flat surfaces is a very difficult task.[32] Despite of these results, caution is required for interpretation of the results because of the imprecision of the Bradford assays mentioned above.

Ion diffusion in Omp2a-filled nanoperforated PLA nanomembrames. Electrochemical impedance spectroscopy (EIS) studies were conducted to monitor changes in the resistance and capacitance caused by the presence of nanopores filled by Omp2a aggregates. Accordingly, the impedance was measured for frequencies ranging from 10^{-2} to $10^{4.5}$ Hz for non-perforated, nanoperforated, and Omp2a-filled nanoperforated PLA NMs using several electrolytes. For all assays, such PLA NMs were supported onto ITO semiconductor electrodes, which exhibit both a high electron density (10^{21} e^- / cm^3) and a good stability in aqueous solution for electrochemical

applications.[33] Stability of bare ITO was essential to retain the charged protein inside the induced nanopores during EIS measurements on Omp2a-filled PLA NMs. It should be emphasized that no protein was lost during EIS measurements on Omp2a-filled PLA NMs. Thus, the concentration of Omp2a immobilized in the perforated PLA NMs, which was analysed by the Bradford assay, was maintained within the same concentration range before and after EIS studies (4.1±1.0 and 5.4±1.54 $\mu g \cdot cm^2$, respectively). The electrolyte concentration interval selected for this study was identical to that previously used by Balme *et al.*[34] to examine the ion transport through hybrid biological/artificial solid-state nanoporous membrane as a function of salt concentration.

Figure 5 displays the Bode and Nyquist plots recorded for ITO substrate and the three PLA NMs, using 0.5 M NaCl aqueous solution. The electric equivalent circuits (EECs) (see Figure 5e) of the bare ITO electrode shows the electrolyte resistance (R_S) connected in series with the capacitance of the double layer semiconductor/electrolyte interface (Q_{dl}), which is consistent with the EEC reported in the literature.[33] The quality of the experimental data fitting to EECs was evaluated by the estimate percentage error associated with each circuit element, being lower than 10% in virtually all cases (Table 2). The R_S parameter is not affected by changes occurring on the electrode surface,[35] whereas the Q_{dl} parameter is often modelled as a constant phase element (CPE) instead of a pure capacitance (C_{dl}) since the phase angle is lower than 90º.[36,37] In addition to the heterogeneity of the electrode surface (*i.e.* roughness, porosity, reactivity), the CPE impedance (Z_{CPE}) is also related to non-uniform diffusion across the interface. That is, Z_{CPE} is defined as $[Q \cdot (j\omega)^n]^{-1}$ and is associated to a pure capacitor for n= 1 or a pure resistor for n= 0. For n= 0.5, it accounts for a diffusion process. Accordingly, the impedance of ITO layer (Figure 5a) consists of a frequency-independent response at high frequencies (R_S), while it steadily increases for frequencies below 10^3 Hz (Q_{dl}; n =

0.97). Moreover, as polymer films are porous materials, two shoulders appear at log |Z| *vs* log f plot for systems covered by PLA membrane. Figure 5a exhibits a broad shoulder between 10 and 10^3 Hz, that corresponds to the parallel association of the membrane resistance (R_M) and the membrane capacitance (Q_M) (Figure 5e). Furthermore, a second shoulder appears at frequencies below 0 Hz, corresponding to the membrane pore resistance (R_p) in parallel with the Q_{dl} of the ITO electrolyte/interface. The electrical response is perfectly adjusted to the electrical circuit (in series) shown in Figure 5e. Both shoulders represent two time constants (τ) in the Bode plot (Figure 5b, phase angle). Regarding the Nyquist spectra (Figures 5c), all three NMs display curves with two semicircles: the starting point of the curve indicates R_S, the first semicircle (at high frequencies) corresponds to R_M and $Q_{M,}$ whereas the second (at low frequencies) corresponds to R_p and Q_{dl}. The offset on the high frequency impedance zone (Figure 5d) shows the two semi-circles from nanoperforated PLA with adhered Omp2a.

Table 2 lists the contribution of each element for the several NMs tested when the electrolyte is a 0.5 M NaCl solution. As it can be seen, the R_M value of PLA membranes drastically decreases when artificial nanopores were induced across the polymer film, varying from 5.99 $k\Omega \cdot cm^2$ (non-perforated PLA) to 883 $\Omega \cdot cm^2$ (perforated PLA). The confinement of aggregates (from Omp2a protein) into PLA nanopores further reduced the membrane resistance to 317 $\Omega \cdot cm^2$, evidencing that the exchange of ions between the working electrode (bare ITO) and the electrolyte is favoured compared to nanoperforated PLA without protein. However, even though Omp2a adsorbed onto non-perforated PLA nanomembranes results in a R_M value of 2.50 $k\Omega \cdot cm^2$, the confinement of aggregates (from Omp2a protein) into PLA nanopores further reduces the membrane resistance to 317 $\Omega \cdot cm^2$, evidencing that the exchange of ions between the working

electrode (bare ITO) and the electrolyte is favoured when Omp2a and nanopores are combined.

Furthermore, the constant phase element related to the polymer membrane, which accounts for the polymer ability to store charge, increases by one order of magnitude after confining Omp2a. Moreover, we observe R_p sensible to changes occurring above the electrode, the value decreasing as follow: non-perforated PLA > nanoperforated PLA > Omp2a-filled nanoperforated PLA, whereas Q_{dl} varies in the opposite order, as expected. Therefore, the pore resistance has dropped down to 16.8% of its initial value (nanoperforated PLA), indicating a better diffusion of ions across the pore-induced membrane. Diffusion of ions is also observed by the reduction of the *n* exponent in the impedance equation from 0.75 to 0.48 (Table 2). Whilst the diffusion of species in a polymer coating is often modelled with Warburg impedance (Z_W),[38] the diffusion processes are controlled by the pore resistance in the present study.

In order to compare the selectivity of the PLA NMs, impedance analyses were recorded using three electrolytes: NaCl, KCl, and $CaCl_2$ solutions with various concentrations (*i.e.* 50, 100, 500 and 1000 mM). A complete description of the results is provided in the Electronic Supporting Information (*i.e.* Nyquist plots are displayed in Figure S8, while the contribution of each element of the fitted EEC is listed in Tables S2-S4). Similarly to the above-described tendency, non-perforated PLA NMs are characterized by high R_M and low Q_M values that vary with the electrolyte concentration but not with the nature of the cation (Figure 6a). Whilst the same trend is observed for nanoperforated PLA NMs, R_M values here decrease by a factor of 8.7 ± 3.5 compared to non-perforated PLA. Thus, the presence of nanopores decreases the membrane resistance and increases the membrane capacitance, regardless the electrolyte. The R_M values for Omp2a-filled nanoperforated PLA NMs, which ranged between 150.9 $\Omega \cdot cm^2$

(in 1 M NaCl) and 2.2 $k\Omega \cdot cm^2$ (in 50 mM KCl), not only decrease with increasing ion concentration but they were also nature dependent.

On the other hand, the conductance ($Gm = 1/R_M$) values for Na^+ electrolyte at 0.5 M NaCl was measured using Omp2a-coated non-perforated PLA NMs. The resulting Gm value, which is 0.30 ± 0.1 mS, is in good agreement with the values obtained for uncoated non-perforated PLA nanomembranes (Figure 6a). This observation is consistent with the fact that the fraction of protein adsorbed onto the nanomembrane is not contributing to the ion transport, that role being essentially attributed to the Omp2a aggregates confined in the nanopores.

Figures 6b and 6c depict the ion preferences of nanoperforated PLA NMs with and without immobilized Omp2a, respectively, in terms of membrane conductivity (σ) against ion concentration in solution. The membrane conductivity (σ) was calculated from Equation 1:

$$\sigma = \frac{L}{R_M A} \quad (1)$$

where σ is the proton conductivity (S/cm), L is the thickness of the membrane ($\times 10^{-5}$ cm); A is the area of the electrode (1 cm^2), and R_M is the membrane resistance of perforated and non-perforated films. As it can be seen, enhanced ion diffusion was achieved for higher ionic concentrations, especially in the case of Omp2a-containing NMs. In addition, Na^+ and Ca^{2+} ions have a stronger affinity towards the porin channel than K^+ ions, within the studied concentration range, with the best discriminative sensitivity for high concentrations of electrolyte (*i.e.* 0.5 or 1 M). Furthermore, ion selectivity between mono and divalent cations is clearly observed for electrolyte concentrations comprised between 100 and 500 mM.

Finally, changes in R_M with the concentration of electrolyte were found to be reversible. Indeed, after going from highly diluted solutions to concentrated ones and

then back to low concentrated solutions, the values for R_M were maintained. This is illustrated in Figure S9 for Omp2a-filled nanoperforated PLA NMs, which displays the variation of R_M with the KCl concentration.

DISCUSSION

Through the development of nanotechnology and molecular engineering, biomimetic devices based on complex biological structures are now emerging at the nanoscale. Within this context, biomimetic artificial channels and pores have been prepared using different techniques, as for example lithography[39] and ion[40] or electron[41] beam sculpting. Besides, supported OM protein-containing NMs can be prepared by spreading vesicles containing the proteins and by chemical or physical immobilization of the OM protein (*e.g.* by incorporating anchor molecules or by promoting hydrophobic protein–substrate interactions, respectively) onto the substrate.[24,42] In spite of those important advances, supported NMs exhibit fundamental drawbacks.

The first arises from the proximity of the artificial NM and the bare solid surface it is deposited onto, which typically is metallic or ceramic. Thus, the NM···substrate distance is usually not sufficiently large to avoid direct contact between the incorporated OM protein and the solid surface, which usually induces protein denaturation. Different strategies have been proposed to reduce and even eliminate this problem. In a seminal work, Römer and Steinem,[43] inserted gramicidin D into suspended lipidic NMs. More specifically, porous alumina substrates with controlled pore diameter were prepared by anodizing electropolished aluminium foils in acidic solutions, followed by dissolution of the remaining aluminium and alumina at the backside of the pores. After coating one side of such porous material with a thin gold layer that was subsequently functionalized to achieve a hydrophobic surface, suspended 1,2-diphytanoyl-*sn*-glycero-3-

phosphocholin NMs were formed, as was proved by EIS measurements.[43] However, direct contact between the OM protein and the solid surface can be avoided using a much simpler approach, which consists on the application of polymeric NMs to reduce the frictional coupling with the inorganic support.[24,33] For instance, in a recent study, we preserved the β-barrel structure of the OM protein in PNMPy-Omp2a NMs, which were obtained by in situ anodic polymerization introducing Omp2a in the monomer-containing generation medium.[23]

The second, and probably more critical, limitation of supported NMs comes from their own lack of self-supported behaviour. As a result, although supported OM protein-containing NMs have numerous potential applications such as electrochemical biosensing, the applicability of self-supported polymeric NMs is up to now less restricted, which makes them attractive not only for biomedical applications (*e.g.* devices for controlled delivery of ions), but also to other technological fields, like nanofluidics.

In recent years, some studies have been devoted to confine porins into nanopores constructed from polymeric membranes. Jovanovic-Talisman *et al.*[44] tethered porins rich in Phe-Gly domains in track-etched polycarbonate membranes with cylindrical nanopores of 30 nm in diameter and 6 μm in length. For this purpose, a thiol-modified tear porin was attached to the gold-layer previously sputtered onto one side of the NM. On the other hand, Kowalczyk *et al.*[45] demonstrated selective transport of proteins across individual biomimetic nuclear pore complexes at the single-molecule level. This was achieved by drilling nanopores into a 20-nm thin free-standing silicon nitride (SiN) membrane with a focused transmission electron microscope beam. After this, nucleoporin-functionalization of the nanopores was performed in a complex three-step

chemical process with hetero-bifunctional cross-linkers, which is similar to that employed for immobilizing DNA onto silicon surfaces.[46]

In this work, nanoperforated PLA FSNMs were fabricated using an approach based on the combination of spin-coating with phase segregation using immiscible PLA:PVA mixtures, and the subsequent removal of PVA domains via selective solvent etching.[29] The quantitative evaluation of this procedure using different conditions has shown that the diameter of the nanopores decreases from 170±73 nm to 65±32 nm if a 90:10 PLA:PVA mixture is prepared under vigorous stirring.[29] In order to reduce the diameter of the nanoperforations (by ~20%), the concentration of PVA in the PLA: PVA mixture was further decreased in this work. Hence, PLA FSNMs with nanopores of 51±22 nm in diameter and similar depths (~100 nm) were obtained using 99:1 PLA:PVA mixtures.

The intrinsic conformational flexibility of OM proteins critically governs their function as elements for selective transport of ions through cell membranes. Polymeric NMs used as domains to accommodate such biomolecules through their immobilization either at the surface, inside the matrix, or inserted into nanopores as in this work, must preserve such conformational flexibility. Accordingly, the movements of NM components (*i.e.* polymer molecules) facilitate and ultimately determine the functionality of the OM protein. These movements largely depend on the flexibility and mechanical properties of the whole NM. Within this context, it should be emphasized that PLA FSNMs are flexible and, indeed, are softer than bulk PLA. The mechanical properties of non-perforated PLA FSNMs prepared using a procedure similar to that employed in this work (*i.e.* spin-coating) were carefully examined by Takeoka and co-workers[47] using a bulging test. These authors observed that NMs with a thickness of 23±5 nm and 60±14 nm swelled gradually and gave almost semicircular deflection until a pressure of approximately 4 kPa and 7 kPa, respectively. The elastic moduli of these

PLA FSNMs were 1.7±0.1 GPa and 3.1±0.5 GPa, respectively. On the other hand, the elastic modulus of ultrathin PLA-mesh systems, which consists of PLA FSNMs collected on stainless steel meshes, was found to gradually increase with the thickness.[48] That is, the modulus grows from 3.5±1.3 GPa to 5.1±1.0 GPa when the thickness increases from 29±1 to 213±2.4 nm, respectively. Interestingly, comparison of the elastic moduli of FSNMs prepared using different polymers indicates that those coming from PLA are amongst the softer ones.[49] According to these reported observations, the elastic modulus of the NMs prepared in this work, which exhibited a thickness of ~110 nm, are expected to be significantly lower than that reported by Eling *et al.*[50] for bulk PLA films (*i.e.* 7-10 GPa for a film thickness of 703±4.4 nm).

The OM porin Omp2a was reconstituted into preformed nanoperforated PLA FSNMs of moderate electrical resistivity (~12 kΩ). Although this value is considerably smaller than the resistance of lipid bilayers (~1 MΩ)[51,52] frequently used to incorporate and study the functionality of OM proteins and ion transport,[52-54] the PLA-Omp2a molecular architecture studied in this work has provided direct evidences of the enormous changes in the response of artificial nanopores when the protein is confined inside. As a consequence of their response, Omp2a-filled nanoporous PLA FSNMs should be considered hybrid biological/artificial nanosystems with very promising permeation properties for many technological, biomedical, and environmental applications.

Incubation of nanoperforated PLA NMs in Omp2a solution led not only to the immobilization of oval protein aggregates onto the surface, but also to their confinement inside the nanopores. Although the mass of protein at the nanoperforated NMs progressively grew with the concentration of Omp2a in the incubation solution, the immobilized oval aggregates followed the same random distribution in all cases. This behaviour is fully consistent with both the experimental observations and the

biophysical model of outer membranes growth of Gram-negative bacteria,[55] which are composed of proteins, phospholipids, lipoproteins, and lipopolysaccharides. Accordingly, patches of the new OM material, which include porins, are added in discrete bursts that evolve in time following a Stokes flow and organize randomly.

Comparison of the EIS results obtained for nanoperforated PLA NMs with and without Omp2a evidences that the OM protein was properly immobilized, retaining the functionality associated to the β-barrel structure. Most importantly, the Omp2a protein was successfully retained during the overall of the EIS analyses within the membrane, and Omp2a-filled nanoperforated PLA NMs exhibit selective transport of ions when the electrolyte concentrations are high. Thus, the transport of Ca^{2+} and Na^{+} was favoured with respect to the transport of K^{+} for electrolyte concentrations higher than 500 mM, this effect increasing with the concentration. This ion affinity becomes less appreciable for low electrolyte concentrations (50 mM). Interestingly, the diffusion of Na^{+} and Ca^{2+} ions are significantly lower for nanoperforated PLA NMs at the highest electrolyte concentration (1 M), evidencing the crucial role played by Omp2a in the transport process. Although porins are not selective because of their pore dimensions (*i.e.* they are too large to be specific), the pore walls are known to have slight preferences for ion permeability.[56] In general, the selectivity of large pores, like those of porins, are associated with two components:[57] *i)* partitioning, an equilibrium between the exclusion and accumulation of ions within the pore; and *ii)* diffusion, a non-equilibrium measure of the intrinsic ion mobility within the pore. The fact that in the present study the best discrimination was obtained for very high electrolyte concentrations (> 0.5 M) should be attributed to the low transport efficiency of the proteins confined inside the pores, which in turn is related with their relative orientations. Thus, the methodology presented in this work does not allow control the orientation of confined protein aggregates. In

order to achieve the maximum transport efficiency, proteins should be oriented with the channel. Our future work in field is focused on controlling the Omp2a orientation during the deposition process that, obviously, is not an easy task.

In a recent work, Balme *et. al.*[34] used commercial polycarbonate membranes, which were 5 μm thick and exhibited nanopores with diameter of 15 nm, to immobilize gramicidin A. The latter is a linear pentadecapeptide that presents an alternating sequence of D and L amino acids defining a right handed β-helix.[58] The head-to-head association of gramicidin A molecules gives ion channels that are selectively permeable to monovalent cations and impermeable to anions, such as Cl^-.[59] Polycarbonate membranes with gramicidin A confined into the nanopores were permeable to K^+ and in a minor proportion to Na^+ and Ca^{2+}, even though the KCl/NaCl diffusion coefficient ratio was comparable to that measured through gramicidin A under biological conditions (*i.e.* lipid bilayers).[34] These results were attributed to the fact the β-helical conformation was kept in the pore centre. Omp2a-filled nanoperforated PLA NMs provide two important improvements with respect to polycarbonate membranes. First, the thickness of the membrane has been reduced from the micrometric to the nanometric scale preserving the free-standing behaviour. Moreover, such a reduction facilitates the movement of the polymer molecules enhancing the flexibility of the NM, which affects positively to the ion transport across the biomolecule. Second, PLA is not only biocompatible, as is polycarbonate, but is also biodegradable. Accordingly, FSNMs made of PLA and Omp2a are very promising for biomedical applications that require completely biodegradable devices for selective ion transport.

Chaaya *et al.*[60] reported the confinement of gramicidin A inside nanopores (diameter 10.6 nm, 5.7 nm and ~2 nm) obtained by track-etching and atomic layer deposition on flexible poly(ethyleneterephthalate) (PET) films. Amazingly, in that case confined

gramicidin A exhibited a better permeability to Cl^- than to Na^+ (*i.e.* the permeability ratio $P_{Na+}/P_{Cl-} < 1$). This behaviour, which is contrary to the selectivity of the channel in biological membranes, was explained by the loss of gramicidin head-to-head association. In biological membranes the impermeability to Cl^- is due to changes in the hydration state near the head-to-head connection between associated gramicidin molecules and in the β-helix structure.[61,62] However in PET membranes, the gramicidin aggregation is dismantled in the solution used for the immobilization, and is not recovered upon confinement inside the nanopore.[60] In order to preserve the operative and functional state of the biomolecule when confined inside nanopores, the protein must retain its folded and assembled form. In this work, the β-barrel structure of the Omp2a porin (Figure S3) has been saved not only because of the formation of a stable PLA–Omp2a interface, but also because of the nanometric thickness of PLA FSNMs. Thus, the confinement of biomolecules inside polymeric NMs avoids the influence of many effects typically associated with bulk polymers. For example, the formation of well-defined multiphasic microdomains (*i.e.* coexisting crystalline and amorphous domains) results in different polymer–biomolecule interfaces since the properties of such domains differ. Also, with respect to NMs, the flexibility and the elastic modulus of bulk films are lower and higher. Accordingly, the formation of stable polymer–biomolecule interfaces is more difficult in bulk films because of the reduction of the polymeric molecules motion. It should be underlined that the thickness of the PET films reported by Chaaya *et al.*[60] was ~5 μm and in this case, the polymer–biomolecule effects should be related to those typically found in systems involving bulk polymers.

CONCLUSIONS

We have examined the feasibility of FSNMs for selective ion transport by integrating an OM protein, Omp2a, into nanoperforated ultra-thin films of PLA. When oval protein aggregates were immobilized inside nanoperforations of diameter 51±22 nm, the resulting PLA NMs showed much higher ion transport activity than nanoperforated films without immobilized Omp2a, especially at high electrolyte concentrations. Hence, the ion affinity of Omp2a-filled nanoperforated PLA NMs increases with the concentration. In addition, ion diffusion of Ca^{2+} and Na^{+} ions through Omp2a-filled nanopores is significantly higher than for K^{+} at concentrations ≥ 500 mM. Overall the results suggest that the novel Omp2a–PLA platform fulfills not only the nanometric dimensional requisite for truly mimicking biological attributes, but also the conditions necessary for designing new NMs for biosensing, nanofluidics and ion-rectifying for energy conversion. This study demonstrates that the bioinspired combination of nanofeatures supported onto polymeric FSNMs with the confinement of OM proteins is a powerful approach that synergistically associates the most important advantages of each component.

ACKNOWLEDGEMENTS

This work was supported by MINECO (MAT2015-69367-R). Support for the research of C.A. was received through the prize "ICREA Academia" for excellence in research funded by the Generalitat de Catalunya. C.M. and E.A.P. thank the Belgian National Fund for Scientific Research for their research associate and senior research associate positions, respectively.

REFERENCES

1. L. Zeng, Z. Yang, H. Zhang, X. Hou, Y. Tian, F. Yang, J. Zhou, L. Li and L. Jiang, *Small*, 2014, **10**, 793–801.

2. H. Daiguji, *Chem. Soc. Rev.*, 2010, **39**, 901–911.

3. M. Ali, B. Yameen, J. Cervera, P. Ramirez, R. Neumann, W. Ensinger, W. Knoll and O. Azzaroni, *J. Am. Chem. Soc.*, 2010, **132**, 8338–8348.

4. B. V. V. S. P. Kumar, K. V. Rao, S. Sampath, S.J. George and M. Eswaramoorthy, *Angew. Chem., Int. Ed*., 2014, **53**, 13073–13077.

5. B. N. Miles, A. P. Ivanov, K. A. Wilson, F. Dogan, D. Japrung and J. Edel, *Chem. Soc. Rev.*, 2013, **42**, 15–28.

6. A. de la Escosura-Muñiz and A. Merkoc-i, *ACS Nano*, 2012, **6**, 7556–7583.

7. S. Balme, J. M. Janot, L. Berardo, F. Henn, D. Bonhenry, S. Kraszewski, F. Picaud and C. Ramseyer, *Nano Lett.*, 2011, **11**, 712−716.

8. M. Ali, S. Nasir, Q. H. Nguyen, J. K. Sahoo, M. N. Tahir, W. Tremel and W. Ensinger, *J. Am. Chem. Soc.*, 2011, **133**, 17307−17314.

9. A. Cazacu, Y. M. Legrand, A. Pasc, G. Nasr, A. Van der Lee, E. Mahon and M. Barboiu, *Proc. Natl. Acad. Sci. U. S. A.*, 2009, **106**, 8117−8122.

10. S. Kim, J. Nham, Y. S. Jeong, C. S. Lee, S. H. Ha, H. B. Park and Y. J. Lee, *Chem. Mater.*, 2015, **27**, 1255−1261

11. S. W. Kowalczyk, T. R. Blosser and C. Dekker, *Trends Biotechnol*., 2011, **29**, 607–614.

12. S. Galdiero, A. Falanga, M. Cantisani, R. Tarallo, M. E. Della Pepa, V. D'Oriano and M. Galdiero, *Curr. Protein Pept. Sci.*, 2012. **13**, 843–854.

13. E. J. Weeber, L. Michael, M. J. Sampson, K. Anflous, D. L. Armstrong, S. E. Brown, J. D. Sweatt and W. J. Craigen, *J. Biol. Chem.*, 2002, **277**, 18891–18897.

14. K. Fischer, A. Weber, S. Brink, B. Arbinger, D. Schünemann, S. Borchert, H. W. Heldt, B. Popp, R. Benz, T. A. Link, C. Eckerskorn and U.-I. Flügge, *J. Biol. Chem.*, 1994, **269**, 25754–25760.

15. J. Cama, H. Bajaj, S. Pagliara, T. Maier and Y. Braun, *J. Am. Chem. Soc.***,** 2015, **137**, 13836–13843.

16. M.–L. Boschiroli, V. Foulongne and D. A. O'Callaghan, *Curr. Opin. Microbiol.*, 2001, **4**, 58-64.

17. G. Roussel, A. Matagne, X. De Bolle, E. A. Perpète and C. Michaux, *Protein Expr. Purif.*, 2012, **83**, 198–204.

18. G. Roussel, E. A. Perpète, A. Matagne, E. Tinti and C. Michaux, *Biotechnol. Bioeng.*, 2013, **110**, 417–423.

19. T. M. Fyles, *Chem. Soc. Rev.*, 2007, **36**, 335−347.

20. W. Meier, C. Nardin and M. Winterhalter, *Angew. Chem., Int. Ed.*, 2000, **39**, 4599−4602.

21. M. Kumar, M. Grzelakowski, J. Zilles, M. Clark and W. Meier, *Proc. Natl. Acad. Sci. U. S. A.*, 2007, **104**, 20719−20724.

22. A. Gonzalez-Perez, K. B. Stibius, T. Vissing, C. H. Nielsen and O. G. Mouritsen, *Langmuir*, 2009, **25**, 10447−10450.

23. X. Hou, W. Guo and L. Jiang, *Chem. Soc. Rev.*, 2011, **40**, 2385−2401.

24. M. M. Pérez-Madrigal, L. J. del Valle, E. Armelin, C. Michaux, G. Roussel, E. A. Perpète and C. Alemán, *ACS Appl. Mater. Interfaces*, 2015, **7**, 1632–1643.

25. X. Zhang, W. Fu, C. G. Palivan and W. Meier, *Sci. Rep.*, 2013, **3**, 2196.

26. B. Teixeira-Dias, C. Alemán, F. Estrany, D. S. Azambuja and E. Armelin, *Electrochim. Acta*, 2011, **56**, 5836−5847.

27. D. Aradilla, F. Estrany and C. Alemán, *J. Phys. Chem. C*, 2011, **115**, 8430−8438.

28. W. Guo, L. Cao, J. Xia, F.-Q. Nie, W. Ma, J. Xue, Y. Song, D. Zhu, Y. Wang and L. Jiang, *Adv. Funct. Mater.*, 2010, **20**, 1339–1344.

29. A. Puiggalí-Jou, J. Medina, L. J. del Valle and C. Alemán, *Eur. Polym. J.*, 2016, **75**, 552-564.

30. J.-Y. Paquet, M. A. Diaz, S. Genevrois, M. Grayon, J. M. Verger, X. de Bolle, J. H. Lakey, J.-J. Letesson and A. Cloeckaert. *J. Bacteriol.* 2001, **183**, 4839–4847.

31. K. Zeth and M. Thein, *Biochem. J.*, 2010, **431**, 13–22.

32. K. Rechendorff, M. B. Hovgaard, M. Foss, V. P. Zhdanov and F. Besenbacher, *Langmuir*, 2006, **22**, 10885–10888.

33. H. Hillebrandt, G. Wiegand, M. Tanaka and E. Sackmann, *Langmuir*,1999, **15**, 8451–8459.

34. S. Balme, F. Picaud, S. Kraszweski, P. Déjardin, J. M. Janot, M. Lepoitevin, J. Capomanes, C. Ramseyer, F. Henn, *Nanoscale*, 2013, **5**, 3961–3968.

35. M. Barreiros dos Santos, S. Azevedo, J. P. Agusil, B. Prieto-Simón, C. Sporer, E. Torrents, A. Juárez, V. Teixeira and J. Samitier, *Bioelectrochemistry*, 2015, **101**, 146–152.

36. X. Qian, N. Gu, Z. Cheng, X. Yang and E. Wang, *Electrochim. Acta*, 2001, **46**, 1829–1836.

37. J.-B. Jorcin, M. E. Orazem, N. Pébère and B. Tribollet, *Electrochim. Acta*, 2006, **51**, 1473–1479.

38. S. Skale, V. Dolecek and M. Slemnik, *Corr. Sci.*, 2007, **49**, 1045-1055.

39. Z. Siwy, and A. Fulinski, A., *Phys. Rev. Lett.*, 2002, **89**, 198103.

40. J. Li, D. Stein, C. McMullan, D. Branton, M. j. Aziz and J. A. Golovchenko, *Nature*, 2001, **412**, 166–169.

41. A. J. Storm, J. H. Chen, X. S. Ling, H. W. Zandbergen and C. Dekker, *Nat. Mater.*, 2003, **2**, 537–540.

42. M. Tanaka and E. Sackmann, *Nature*, 2005, **437**, 656–663.

43. W. Römer and C. Steinem, *Biophys. J.*, 2004, ***86***, 955–965.

44. T. Jovanovic-Talisman, J. Tetenbaum-Novatt, A. S. McKenney, A. Zilman, R. Peters, M. P. Rout and B. T. Chait, *Nature*, 2009, **457**, 1023–1027.

45. S. W. Kowalczyk, L. Kapinos, T. R. Blosser, T. Magalhães, P. van Nies, R. T. H. Lim and C. Dekker, *Nat. Nanotechnol.*, 2011, **6**, 433–438.

46. L. Jin, A. Horgan and R. Levicky, *Langmuir*, 2003, **19**, 6968–6975.

47. Y. Okamura, K. Kabata, M. Kinoshita, D. Saitoh and S. Takeoka, *Adv. Mater.*, 2009, **21**, 4388–4392.

48. T. Fujie, L. Ricotti, A. Desii, A. Menciassi, P. Dario and V. Mattoli, *Langmuir*, 2011, **27**, 13173–13182.

49. M. M. Pérez-Madrigal, E. Armelin, J. Puiggalí and C. Alemán, *J. Mater. Chem. B*, 2015, **3**, 5904–5932.

50. B. Eling, S. Gogolewski and A. J. Pennings, *Polymer*, 1982, **23**, 1587–1593.

51. V. Atanasov, N. Knorr, R. S. Duran, S. Ingebrandt, A. Offenhäusser, W. Knoll and I. Köper, *Biophys. J.*, 2005, **89**, 1780–1788.

52. S. Gritsch, P. Nollert, F. Jähnig and E. Sackmann, *Langmuir*, 1998, **14**, 3118–3125.

53. Z.-W. Zhu, Y. Wang, X. Zhang, C.-F, Sun, M.-G. Li, J.-W. Yan and B.W. Mao, *Langmuir*, 2012, **28**, 14739–14746.

54. K. Sugihara, J. Vörös and T. A. Zambelli, *ACS Nano*, 2010, **4**, 5047–5054.

55. T. S. Ursell, E. H. Trepagnier, K. C. Huang and J. A. Therit, *PLoS Comput. Biol.*, 2012, **8**, e1002680.

56. V. M. Aguilella, M. Queralt-Martín, M. Aguilella-Arzo and A. Alcaraz, *Integr. Biol. (Camb).*, 2011, **3**, 159–172.

57. M. L. López, M. Aguilella-Arzo, V. M. Aguilella and A. Alcaraz, *J. Phys. Chem. B*, 2009, **113**, 8745–8751.

58. R. R. Ketchem, W. Hu and T. A. Cross, *Science*, 1993, **261**, 1457–1460.

59. A. Chernyshev, R. Pomès and S. Cukierman, *Biophys. Chem.*, 2003, **103**, 179–190.

60. A.A. Chaaya, M. Le Poitevin, S. Cabello-Aguilar, S. Balme, M. Bechelany, S. Kraszewski, F. Picaud, J. Cambedouzou, E. Balanzat, J.-M. Janot, T. Thami, P. Miele and P. Dejardin, *J. Phys. Chem. C*, 2013, **117**, 15306−15315.

61. J. F. Hinton, J. Q. Fernandez, D. C. Shungu and F. S. Millett, *Biophys. J.*, 1989, **55**, 327−330.

62. T. W. Allen, O. S. Andersen and B. Roux, *Biophys. Chem.*, 2006, **124**, 251−267.

CAPTIONS TO FIGURES

Figure 1. TEM micrographs of Omp2a trimeric units (short red line) and higher aggregates (large red line) derived from solutions stained with 2% uranyl acetate. Scale bar of the high resolution micrographs: 10 nm. The effective diameter (D_{eff}, in nm) distribution for both Omp2a trimers and aggregates are also displayed (top and bottom, respectively).

Figure 2. (a) 3D AFM height images coloured with phase skin: PLA-PVA NM obtained using a 99:1 PLA:PVA mixture (left) and nanoperforated PLA NM derived from PLA-PVA *via* selective water etching; (b) High magnification SEM micrographs, pore diameter distribution, and AFM height images (2×2 and 0.5×0.5 μm^2) with their corresponding phase images for nanoperforated PLA NM obtained using 99:1 PLA:PVA mixtures. (c) Photograph showing a floating nanoperforated PLA FSNM.

Figure 3. (a) Average contact angle (CA) and root-mean-square roughness (Rq) values (5×5 μm^2 surface area) determined for ITO substrate, non-perforated PLA NMs, nanoperforated PLA before and after Omp2a incubation. Greek letters on the columns refer to significant differences ($p < 0.05$) when the 1 way ANOVA and Tukey's multiple comparisons test are applied: α *vs* ITO, β *vs* non-perforated PLA and δ *vs* nanoperforated-PLA. Images of the drops onto nanoperforated PLA with (bottom) and without (top) immobilized Omp2a are also displayed. (b) SEM micrographs of perforated PLA NMs after Omp2a immobilization: low and high magnifications at left and right, respectively. Dashed arrows illustrate the presence of big protein aggregates. (c) AFM height and their corresponding phase images (window: 0.5 × 0.5 μm^2) of nanoperforated PLA after Omp2a incubation. Several representative cross-sectional profiles showing the topography and dimensions of the nanopores (dashed circles) are

also displayed. In all samples, incubation was performed considering a 0.5 mg/mL Omp2a solution.

Figure 4. (a) 3D AFM phase images of the skin surfaces of perforated PLA NMs before (left) and after (right) incubation with a 0.5 mg/mL Omp2a solution. Oval protein aggregates are clearly identified at the surface and inside the nanopores. Diameter (b) and height (c) distributions of the protein aggregates observed in (a). (d) Results from Bradford assays for non-perforated (incubation with a 0.50 mg/mL Omp2a solution) and perforated (incubation with 0.5, 0.25 and 0.125 mg/mL Omp2a solutions). Grey spheres represent the retention efficiency (in %) while black bars correspond to the mass of protein entrapped per unit of area ($\mu g/cm^2$). Error bars indicate the standard deviation and greek letters on the columns refer to significant differences ($p < 0.05$) in protein entrapped per unit of area ($\mu g/cm^2$) when the 1way ANOVA and Tukey's multiple comparisons test are applied: α *vs* non-perforated PLA, β *vs* nanoperforated-PLA incubated with 0.25 mg/mL and δ *vs* nanoperforated-PLA incubated with 0.125 mg/mL.

Figure 5. Bode (a, b) and Nyquist (c, d) plots of ITO (circle), non-perforated PLA (square), nanoperforated PLA (triangle), Omp2a-coated non-perforated PLA (cross) and Omp2a-filled nanoperforated PLA (diamond) in NaCl 0.5 M; (d) corresponds to an amplified area from (c), for better visualization of high frequency zone. Symbols correspond to experimental data, while lines are fitted curves according to EEC. (e) EEC used for fitting the experimental data from EIS measurements: R_S is the electrolyte resistance; Q_M and R_M are the membrane constant phase element and resistance, respectively; Q_{dl} and R_p are the double layer constant phase element and the pore resistance, respectively. The depicted surfaces are (left) ITO and (right) non-perforated

PLA, nanoperforated-PLA and Omp2a-filled nanoperforated PLA NMs (from top to bottom).

Figure 6. (a) Comparison of the NM conductance ($Gm = 1/R_M$) values for Na^+ (grey), K^+ (red), and Ca^{2+} (blue) electrolytes at different concentrations. In most of the cases, values are the mean of 3 samples and their standard deviation. Greek letters on the columns refer to significant differences ($p < 0.05$) when the 2way ANOVA and Tukey's multiple comparisons test are applied: *α vs* non-perforated PLA, *β vs* nanoperforated-PLA and *δ vs* Omp2a-filled nanoperforated PLA. Dependence of the conductivity (σ; Eqn 1) as a function of the ion concentration in solution for (b) Omp2a-filled nanoperforated and (c) nanoperforated PLA NMs. Non-perforated PLA membrane conductivities are below the dotted orange line. In general the values are the mean of three samples and their standard deviation.

Table 1. Physical parameters of non-perforated and perforated PLA NMs derived from 90:10 and 99:1 PLA:PVA mixtures: Average diameter of the nanopores (ϕ), root-mean-square roughness (Rq) (5×5 μm^2 surface area) and film thickness (L), which also corresponds to the depth of the pores.

NM	ϕ (nm)	Rq (nm)	L (nm)
90:10 perforated PLA	67±31	106±8	114±11
99:1 perforated PLA	51±22	21±3	110±7
Non-perforated PLA	-	1.7±0.2	116±14

Table 2. Resistances (R) and constant phase elements (CPE) for each sample, analysed in NaCl 0.5 M solution, from fitting parameters obtained with the EEC displayed in Figure 5e. The percentage error associated to each circuit element is included in parentheses.

	R_S ($\Omega \cdot cm^2$)	CPE_M ($Fcm^{-2} \cdot s^{n-1}$)	n	R_M ($\Omega \cdot cm^2$)	CPE_{dl} ($Fcm^{-2} \cdot s^{n-1}$)	n	R_I ($\Omega \cdot cm^2$)
Bare ITO	48.5 (0.75)	$7.63 \cdot 10^{-6}$ (0.57)	0.97 (0.13)				
Non-perforated PLA	56 (1.15)	$3.15 \cdot 10^{-6}$ (4.68)	0.92 (1.2)	$5.99 \cdot 10^{3}$ (5.37)	$1.54 \cdot 10^{-5}$ (1.22)	0.79 (1.23)	$135.5 \cdot 10^{3}$ (1.88)
Non-perforated PLA Omp2a-coated	64.3 (1.62)	$5.37 \cdot 10^{-5}$ (12.6)	0.76 (1.5)	$2.5 \cdot 10^{3}$ (20.2)	$3.11 \cdot 10^{-5}$ (6.16)	0. 99 (1.23)	$18.32 \cdot 10^{3}$ (5.3)
Nanoperforated PLA	36.9 (1.9)	$6.41 \cdot 10^{-5}$ (5.29)	0.51 (1.17)	883 (4.78)	$6.56 \cdot 10^{-5}$ (0.83)	0.75 (0.77)	$26.8 \cdot 10^{3}$ (1.23)
Omp2a-filled nanoperforated PLA	56.1 (1.89)	$2.46 \cdot 10^{-5}$ (13.14)	0.96 (2.95)	317 (6.22)	$7.54 \cdot 10^{-4}$ (3.12)	0.48 (2.34)	$4.49 \cdot 10^{3}$ (6.44)

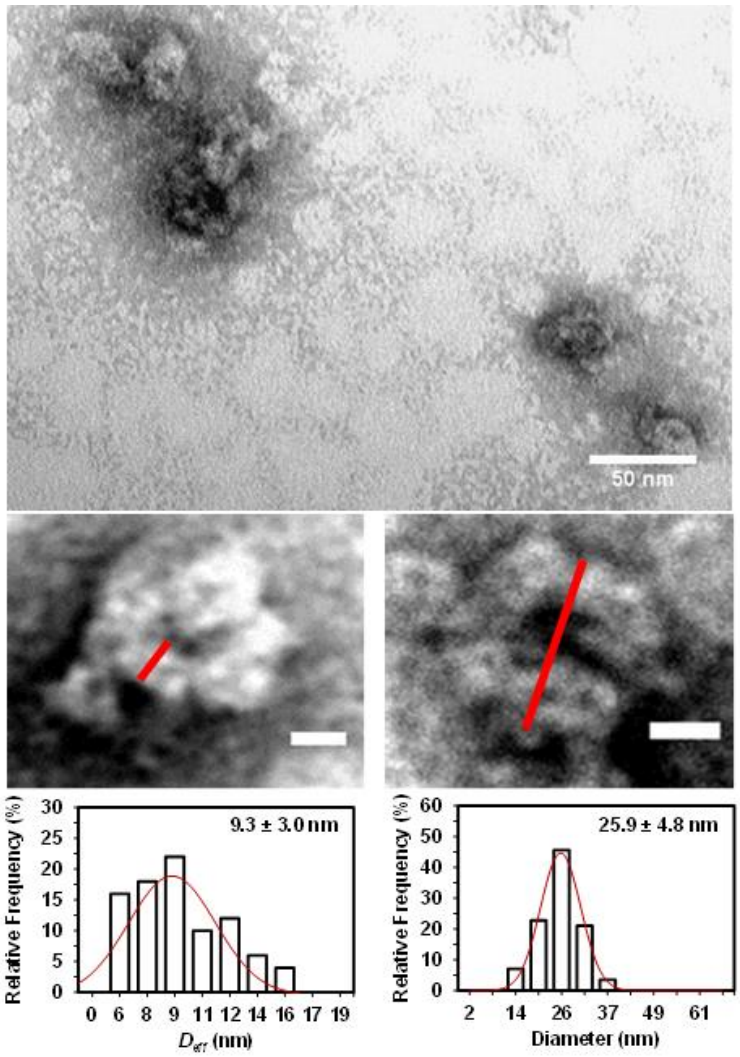
50 nm
Relative Frequency (%)
9.3 ± 3.0 nm
0 6 8 9 11 12 14 16 17 19
D_{eff} (nm)
Relative Frequency (%)
25.9 ± 4.8 nm
2 14 26 37 49 61
Diameter (nm)

Figure 1

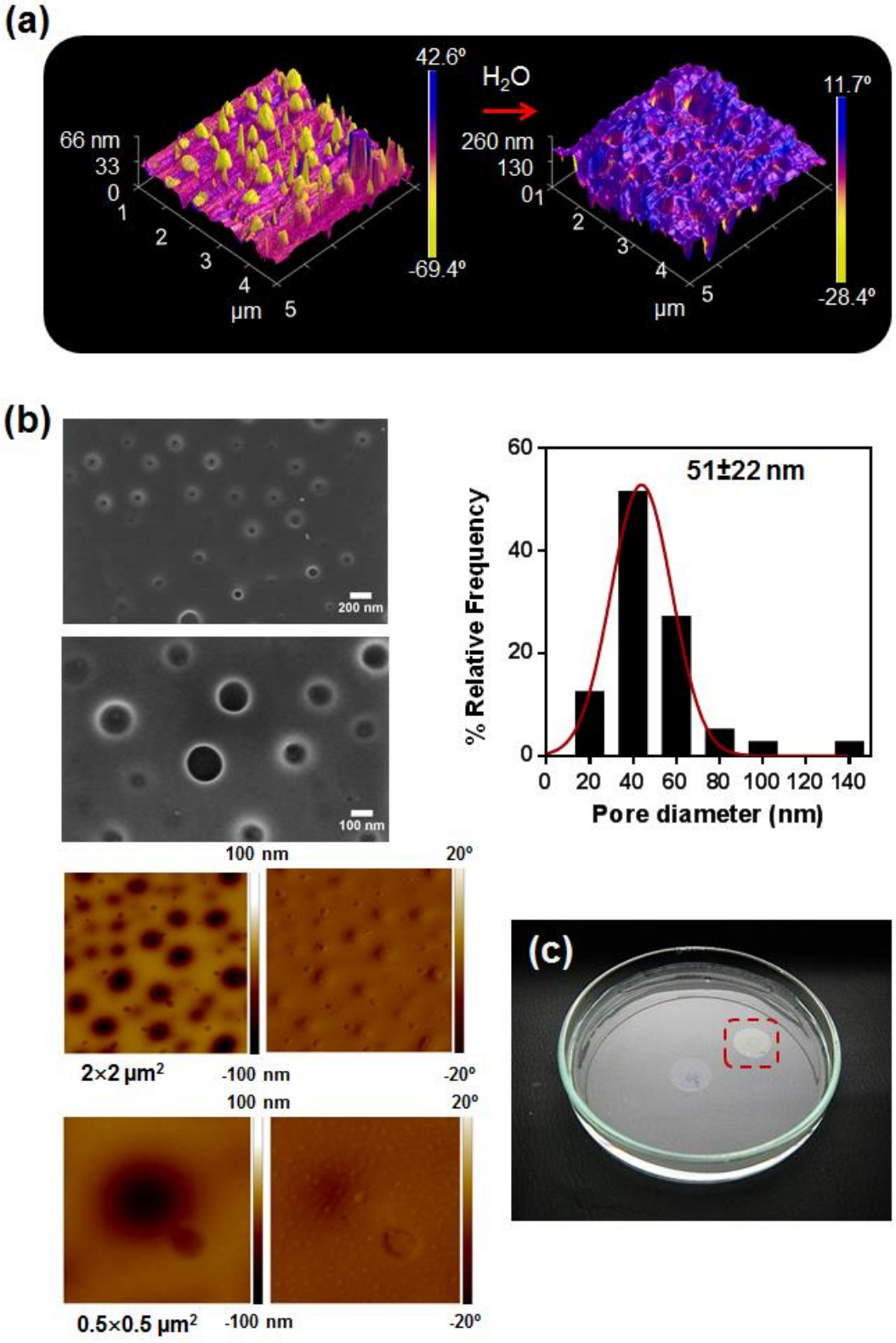
(a)
42.6°
H2O
11.7°
66 nm
33
0
260 nm
130
0
-69.4°
-28.4°
μm
(b)
200 nm
100 nm
51±22 nm
% Relative Frequency
Pore diameter (nm)
100 nm
20°
2×2 μm2
-100 nm
-20°
0.5×0.5 μm2
(c)

Figure 2

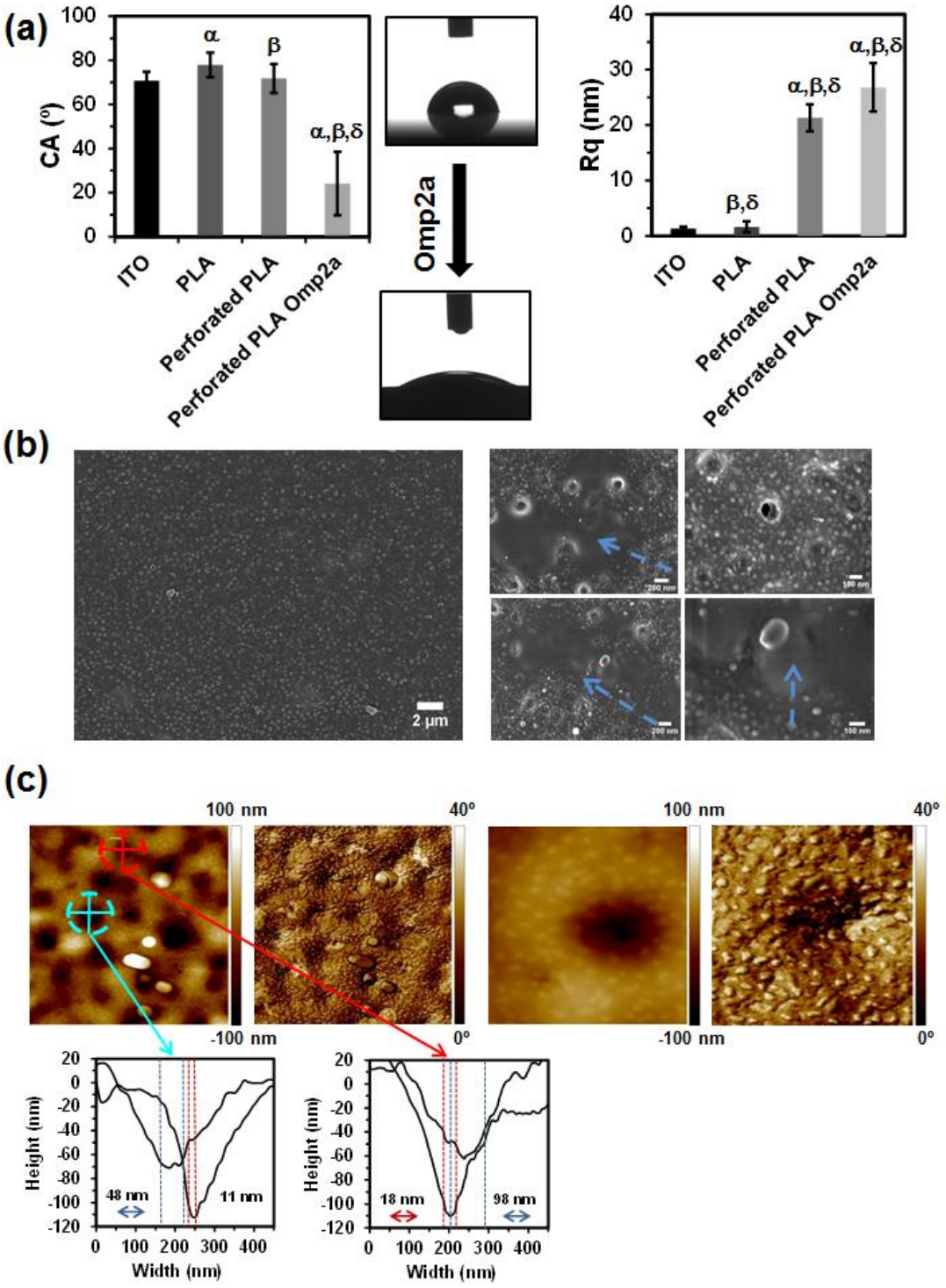
(a)
CA (°)
100
80
60
40
20
0
α
β
α,β,δ
ITO
PLA
Perforated PLA
Perforated PLA Omp2a
Omp2a
Rq (nm)
40
30
20
10
0
β,δ
α,β,δ
α,β,δ
ITO
PLA
Perforated PLA
Perforated PLA Omp2a
(b)
2 µm
(c)
100 nm
40°
-100 nm
0°
100 nm
40°
-100 nm
0°
Height (nm)
20
0
-20
-40
-60
-80
-100
-120
48 nm
11 nm
0
100
200
300
400
Width (nm)
Height (nm)
18 nm
98 nm
Width (nm)

Figure 3

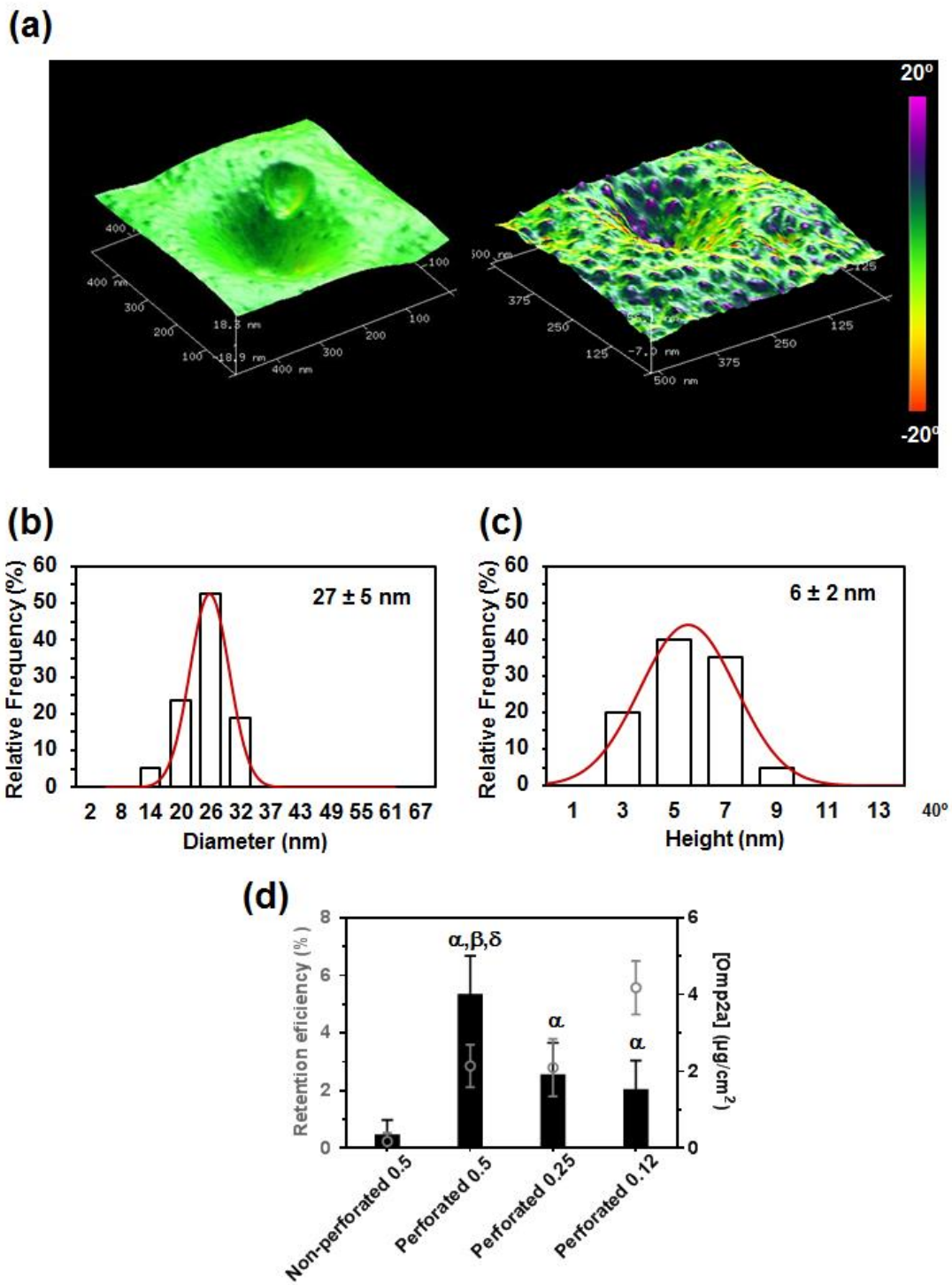
(a)
20°
-20°
(b)
Relative Frequency (%)
27 ± 5 nm
Diameter (nm)
(c)
Relative Frequency (%)
6 ± 2 nm
Height (nm)
40°
(d)
Retention eficiency (%)
[Omp2a] (µg/cm²)
α,β,δ
α
α
Non-perforated 0.5
Perforated 0.5
Perforated 0.25
Perforated 0.12

Figure 4

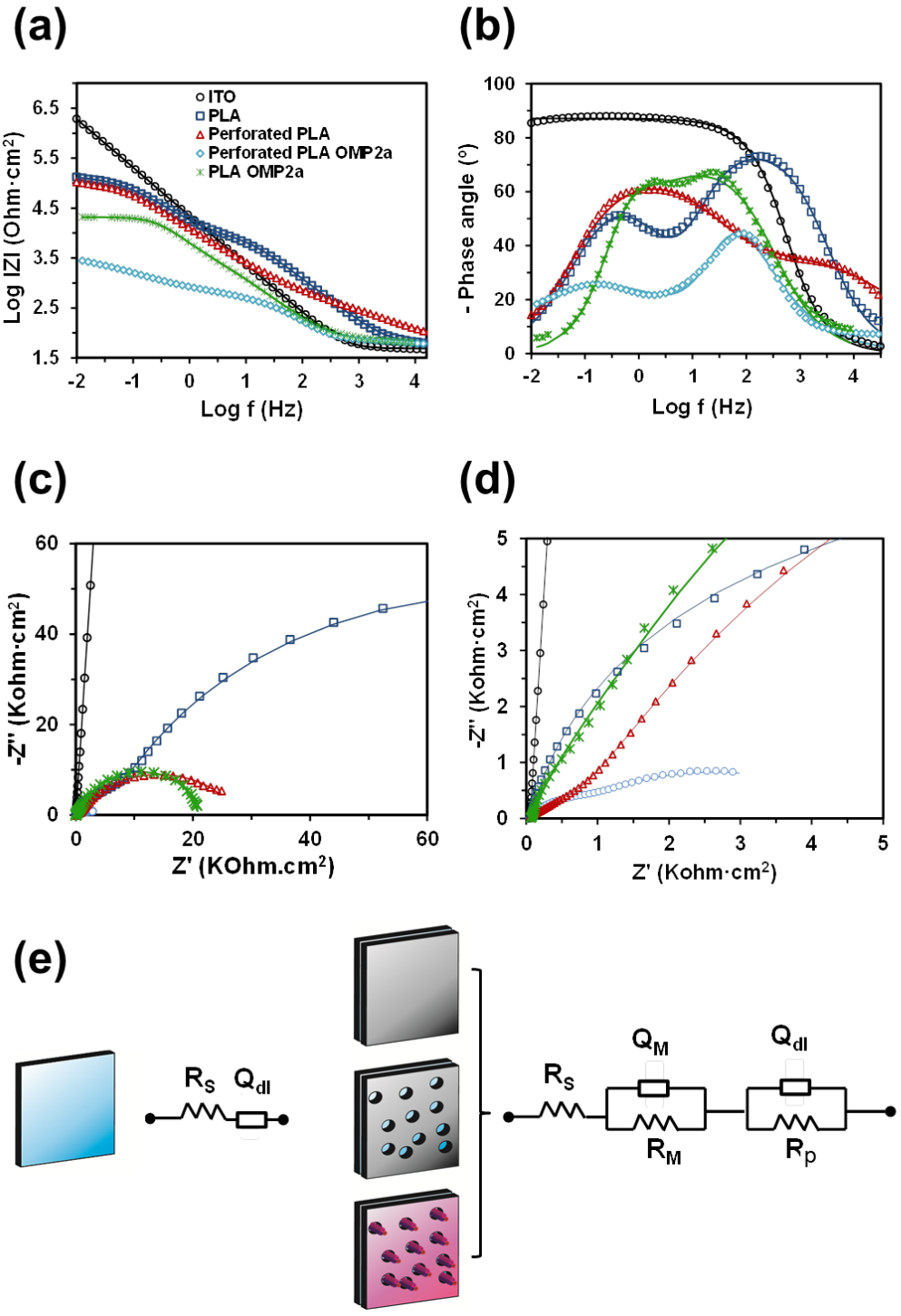
(a)
ITO
PLA
Perforated PLA
Perforated PLA OMP2a
PLA OMP2a
Log |Z| (Ohm·cm²)
Log f (Hz)
(b)
- Phase angle (°)
Log f (Hz)
(c)
-Z'' (Kohm·cm²)
Z' (KOhm.cm²)
(d)
-Z'' (Kohm·cm²)
Z' (Kohm·cm²)
(e)
Rs Qdl
Rs
QM
Qdl
RM
Rp

Figure 5

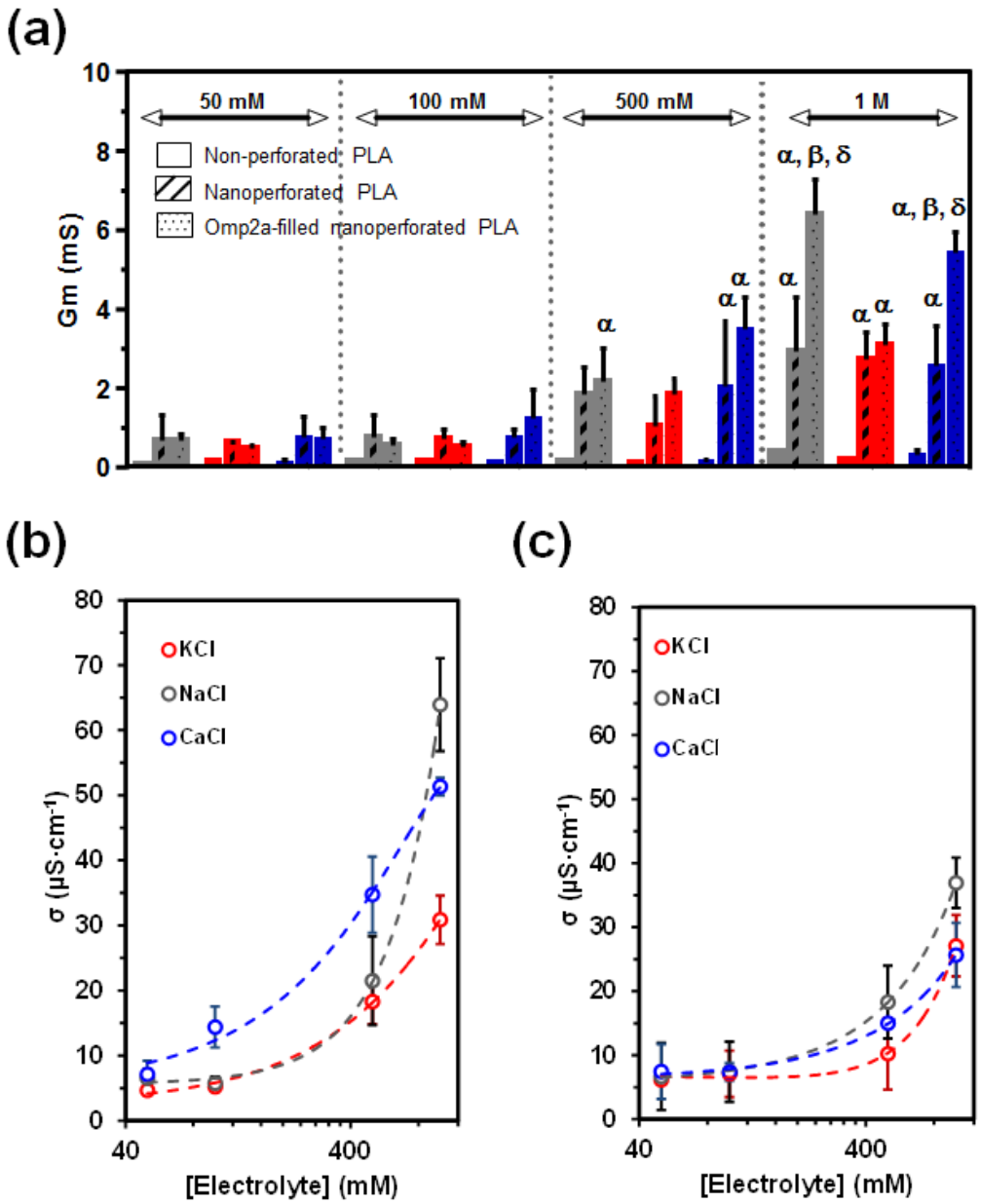
(a)
50 mM
100 mM
500 mM
1 M
Non-perforated PLA
Nanoperforated PLA
Omp2a-filled nanoperforated PLA
Gm (mS)
α
α, β, δ
(b)
(c)
KCl
NaCl
CaCl
σ (μS·cm⁻¹)
[Electrolyte] (mM)

Figure 6